Electronic Supplementary Information

A novel bifunctional catalyst for overall water electrolysis: nano $Ir_xMn_{(1-x)}O_y$ hybrids with $L1_2$-$IrMn_3$ phase

Zhandong Ren,‡ Yanyan Wang,‡ Hucheng Jiang, Hongwei Jiang, Miaojie Tian, Ye Liu, Juanjuan Han,* Hua Fang and Yuchan Zhu*

School of Chemical and Environmental Engineering, Wuhan Polytechnic University, Wuhan, 430023, P. R. China.

‡ Z.D.R. and Y.Y.W. contributed equally to this work.

* Corresponding author:

Yuchan Zhu, Professor, School of Chemical and Environmental Engineering, Wuhan Polytechnic University, Wuhan, 430023, P. R. China.

E-mail: zhuyuchan@163.com. Tel.: 86-27-83943956.

Juanjuan Han, Professor, School of Chemical and Environmental Engineering, Wuhan Polytechnic University, Wuhan, 430023, P. R. China.

E-mail: jjhan@whu.edu.cn. Tel.: 86-27-83943956.

1. Experimental methods

1.1 Chemicals and materials

Chloroiridic acid ($H_2IrCl_6 \cdot 6H_2O$, AR), manganese nitrate ($Mn(NO_3)_2$, AR), acetone (CH_3COCH_3, AR), ethanol (C_2H_5OH, AR), oxalic acid ($C_2H_2O_4$, AR), n-butanol (C_4H_9OH, AR), sulphuric acid (H_2SO_4, AR) and titanium foil (Ti, 99.999%) were purchased from Sinopharm Chemical Reagent Co. Ltd., Shanghai, China. Commercial Pt/C (40 wt% and 60 wt% loading, 2-5 nm Pt size) was purchased from Johnson Matthey Co. Ltd. All reagents were analytical grade and used without further purification. Argon gas (99.999%) and oxygen gas (99.9%) was purchased from Ming-Hui Company. The water (18.25 MΩ cm^{-1}) used in all experiments was prepared by passing through an ultra-pure purification system.

1.2 Preparation of $Ir_xMn_{(1-x)}O_y$ hybrids

Titanium (Ti) foil is used as the electrode substrate, and the area is 1×1 cm. In order to remove impurities and oil stains on the surface of the Ti foil, the Ti foil was cleaned in acetone, ultrapure water and ethanol respectively. Finally, the clean Ti foil was placed in oxalic acid with a mass fraction of 10 % and treated at 95 ℃ for 2 h, and then cleaned and dried for later use.

As shown in scheme 1, $Ir_xMn_{(1-x)}O_y$ hybrids based on Ti foil was prepared by sol-gel and thermal decomposition method without the use of surfactants. The detailed experimental steps are as follows. A typical $Ir_xMn_{(1-x)}O_y$ hybrids (x=0.2) electrode is prepared by the following detailed steps. 0.0110 g $H_2IrCl_6 \cdot 6H_2O$ and 0.0088 g

$Mn(NO_3)_2$ were respectively added into the mixed solvent of ethanol and n-butanol with a volume ratio of 1:1. The total metal ion concentration is 0.02 mol L^{-1}. Magnetic stirring continuously for 24 h to form hydrosol. After the solution is uniformly dispersed by ultrasonic, 25 μL of the solution is dripped onto the Ti foil. When the surface solvent is completely volatilized, it is calcined at 400 ℃ in the mixed gas of Ar-O_2 (10 % O_2) for 1h. The $Ir_xMn_{(1-x)}O_y$ hybrids (x=0.2) electrode can be obtained through the above preparation steps. The loading of Ir is about 19.2 μg cm^{-2}. For different proportions of $Ir_xMn_{(1-x)}O_y$ hybrids electrodes, the preparation process is as follows. At first, while keeping the total metal ion concentration at 0.02 mol L^{-1}, the atomic ratios of Ir and Mn were adjusted to 1:9, 2:8, 3:7, 5:5, 6:4 and 8:2, respectively, to obtain $Ir_xMn_{(1-x)}O_y$ hybrids with different ratios. The loading of Ir is about 9.6 ~ 76.9 μg cm^{-2} for different ratios of $Ir_xMn_{(1-x)}O_y$ hybrids.

1.3 Preparation of IrO_2 and Ir

IrO_2 was prepared by the common thermal decomposition method. Accurately prepare H_2IrCl_6 solution with concentration of 0.02 mol L^{-1}, and its solvent is ethanol-n-butanol mixed solution with volume ratio of 1:1. The solution was stirred for 2 h so that it was mixed evenly. Transfer 5 μL solution and evenly coat it on the Ti foil. After the surface solvent is completely volatilized, it is calcined at 400 ℃ in air atmosphere for 1h to obtain the IrO_2 electrode. Similarly, the Ir electrode can be obtained by calcining at 400°C for 1h in argon atmosphere. The loading of Ir is about 19.2 μg cm^{-2}.

1.4 Preparation of Mn_2O_3

Mn_2O_3 was prepared by the common thermal decomposition method. Accurately prepare $Mn(NO_3)_2$ solution with concentration of 0.02 mol L^{-1}, and its solvent is ethanol-n-butanol mixed solution with volume ratio of 1:1. The solution was stirred for 2 h so that it was mixed evenly. Transfer 40 μL solution and evenly coat it on the Ti foil. After the surface solvent is completely volatilized, it is calcined at 400 ℃ in air atmosphere for 1h to obtain the Mn_2O_3 electrode. The loading of Mn is about 22.0 μg cm^{-2}.

1.5 Preparation of 40 wt% Pt/C and 60 wt% Pt/C

Add 1 mg of commercial 40 wt% Pt/C or 60 wt% Pt/C sample to 1 mL of 0.05 wt% nafion-ethanol solution, and ultrasonically disperse uniformly. Pipette 48 μL of catalyst ink droplets on a Ti foil with an electrode area of 1.0 cm^2 to prepare a 40wt% Pt/C electrode. The loading of Pt is about 19.2 and 28.8 μg cm^{-2} for the 40 wt% Pt/C and 60 wt% Pt/C, respectively.

1.6 Material characterization

X-ray diffraction (XRD) patterns were acquired on an XRD-7000 X-ray diffractometer (Shimadzu, Japan). Transmission Electron Microscopy (TEM) were conducted on an JEM-2100F (JEOL, Japan). Scanning Electron Microscope (SEM) images were taken with a ΣIGMA field-emission SEM (Zeiss, Germany). X-ray photoelectron spectrometry (XPS: ESCLAB 250Xi, Thermo Fisher Scientific, The

United States) with monochromatized Al Kα radiation was used to analyze the electronic properties. Analysis of the composition of the electrode was carried out by X-ray fluorescence (XRF: EDX-7000, Shimadzu, Japan).

1.7 Electrochemical measurements

The electrochemical experiments were carried out in a typical three-electrode electrochemical cell with a carbon paper as a counter electrode (TGP-H-090, Toray, Japan). The reference electrode is $Hg/Hg_2SO_4/K_2SO_4$(0.1 M) and Hg/HgO/KOH(1.0 M) (R0501, Tianjin Aida Hengsheng Technology Development Co., Ltd, China) respectively for acidic and alkaline solutions. Cyclic voltammetry (CV) measurements were performed in Ar-saturated 0.5 M H_2SO_4 solution at the scan rate of 100 mV s^{-1}. The activities of hydrogen evolution reaction (HER) and oxygen evolution reaction (OER) were characterized by linear voltammetry scanning (LSV) in 0.5 M H_2SO_4 or 1.0 M KOH solution at a scanning speed of 5 mV s^{-1}. The analysis of electrochemical surface area (ECSA) is calculated by double-layer capacitance (C_{dl}). At first, CV scanning is performed at different scanning speeds (10, 30, 50, 70, 90, 100 mV s^{-1}) to obtain the current of C_{dl}. Secondly, the double-layer current at 0.35 V is linearly fitted to the scanning rate, and its slope is the C_{dl}. Further divide the C_{dl} by the capacitance constant (C_{ref}, 60 mC cm^{-2}) to obtain ECSA. Electrochemical stability testing is performed by two methods. Electrochemical stability testing is performed by two methods. One test method is to determine electrochemical stability by comparing HER activity before and after CV by a continuous scan of 1000 circles. Another stability test method is to continuously test HER activity at a fixed potential for 10 h. Electrochemical impedance spectroscopy (EIS) was recorded under the condition of frequency of 100 mHz ~ 100 kHz and ac voltage amplitude of 10 mV. For HER reaction, EIS spectrum was measured at an overpotential of 10 mV. While for OER reaction, EIS spectrum was measured at an overpotential of 300 mV. For the overall water splitting capability, a two-electrode system with $Ir_xMn_{(1-x)}O_y$ hybrids electrodes

as anode (Load: 0.1 mg cm^{-2}) and cathode (Load: 0.02 mg cm^{-2}) was constructed in 0.5 M H_2SO_4 solution, denoted as $Ir_xMn_{(1-x)}O_y$ hybrids // $Ir_xMn_{(1-x)}O_y$ hybrids. A comparative evaluation of Pt/C // IrO_2 water electrolyzer composed of Pt/C (cathode) (Load: 0.02 mg cm^{-2}) and IrO_2 (anode) (Load: 0.1 mg cm^{-2}) was carried out in 0.5 M H_2SO_4 solution. The stability of the overall water splitting is maintained for 10 h at the potential of 1.55 V.

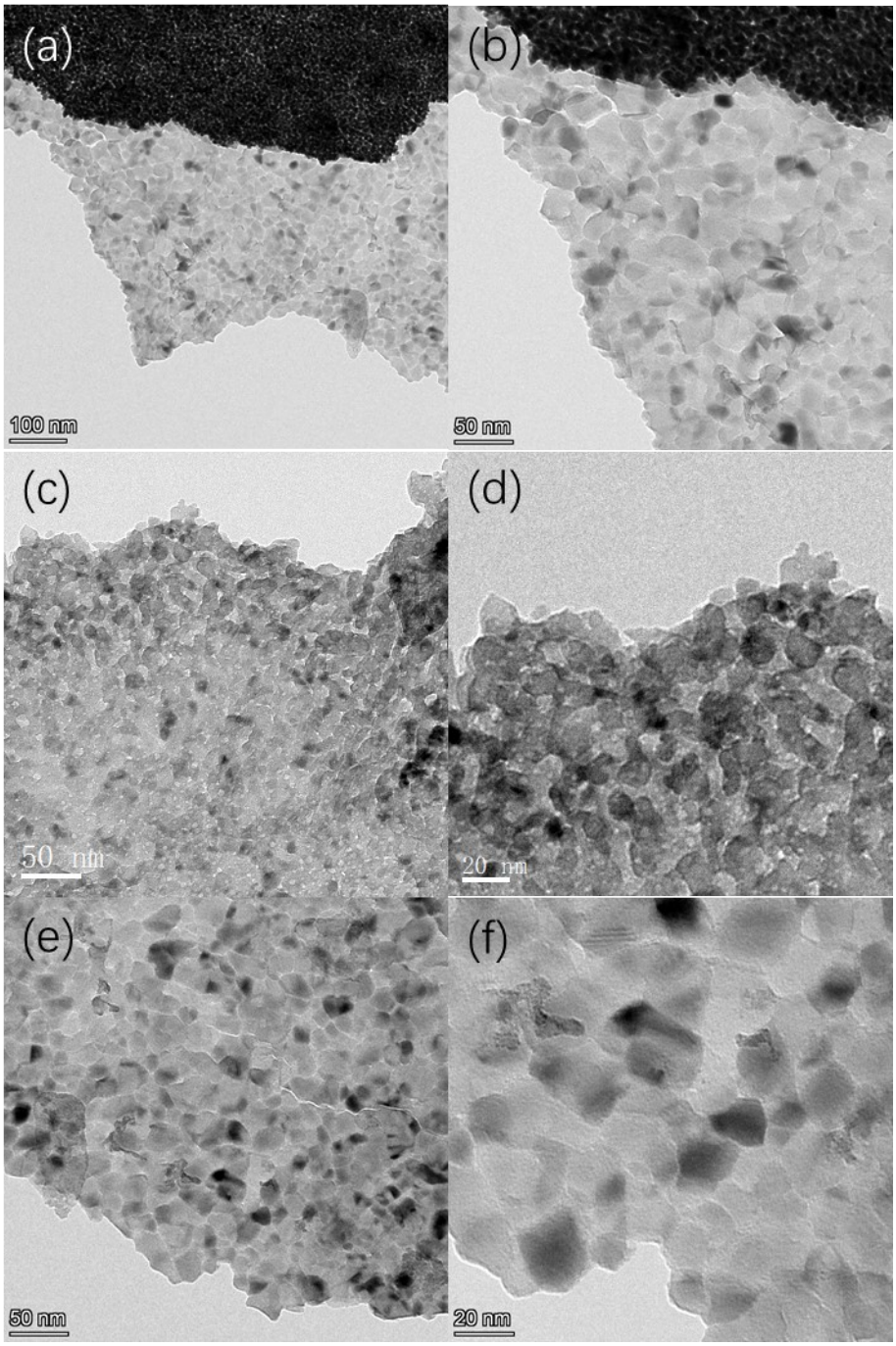

Figure S1 TEM images of $Ir_{0.2}Mn_{0.8}O_y$ hybrids (a-b). TEM images of upper layer (c-d) and underlying layers (e-f) of $Ir_{0.2}Mn_{0.8}O_y$ hybrids.

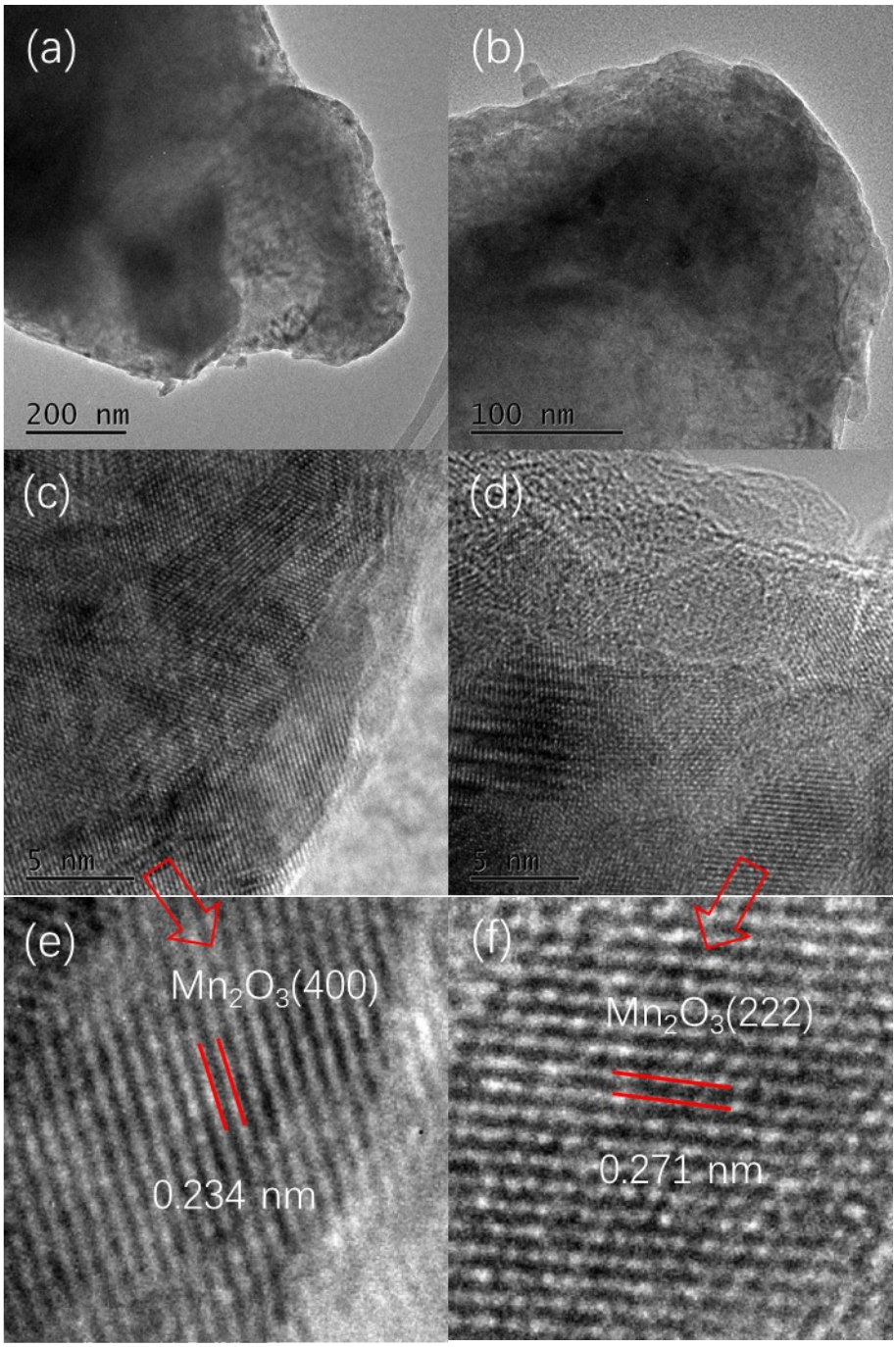

Figure S2 TEM and HRTEM images of Mn_2O_3.

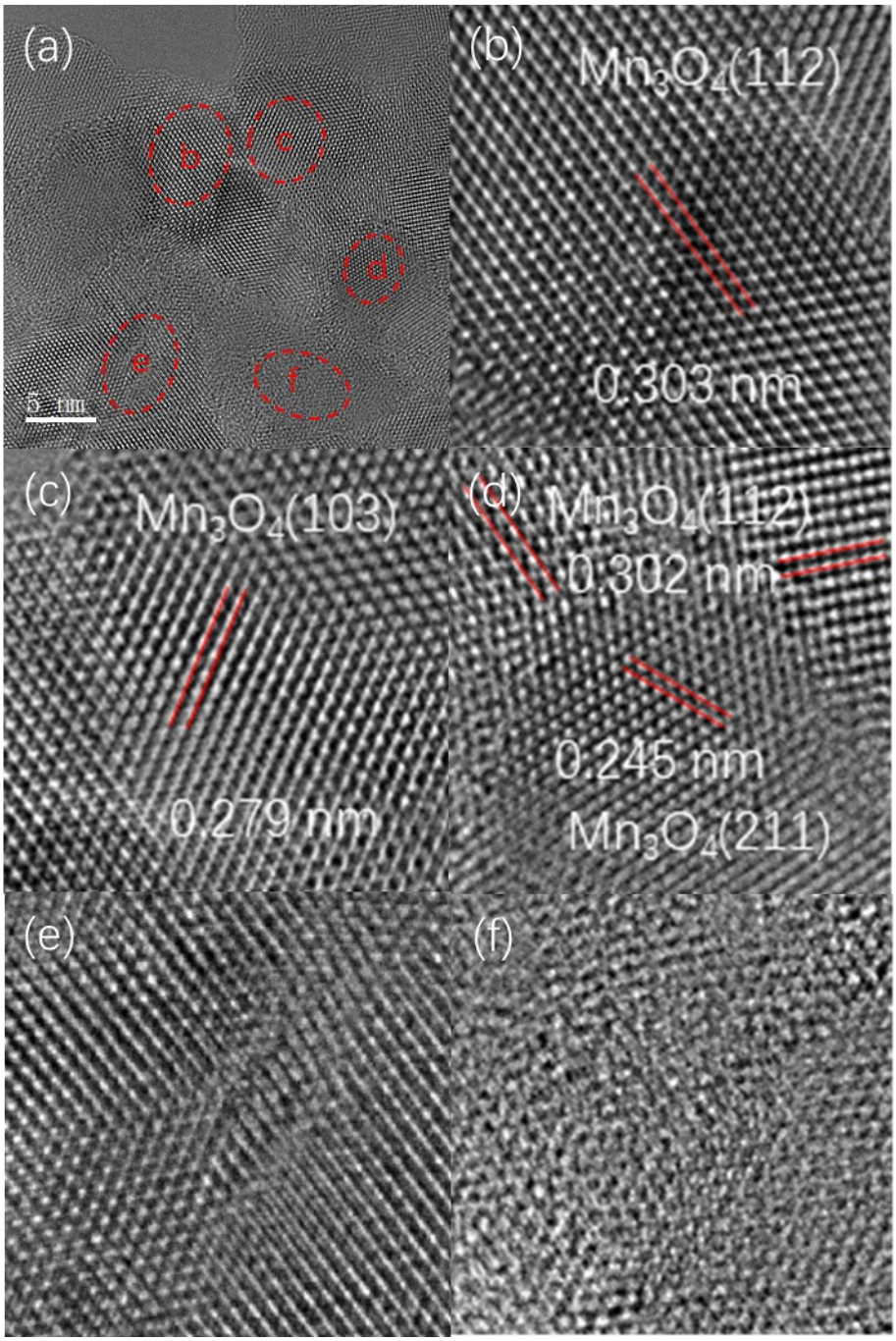

Figure S3 Lattice structures of Mn_3O_4 in the bottom layer of $Ir_{0.2}Mn_{0.8}O_y$ hybrids.

In Fig. S3 a-d (ESI†), the (112) and (103) crystal planes of Mn_3O_4 can be clearly observed. More importantly, a large number of lattice defects and amorphous regions can be clearly observed in Fig. S3 e-f (ESI†).

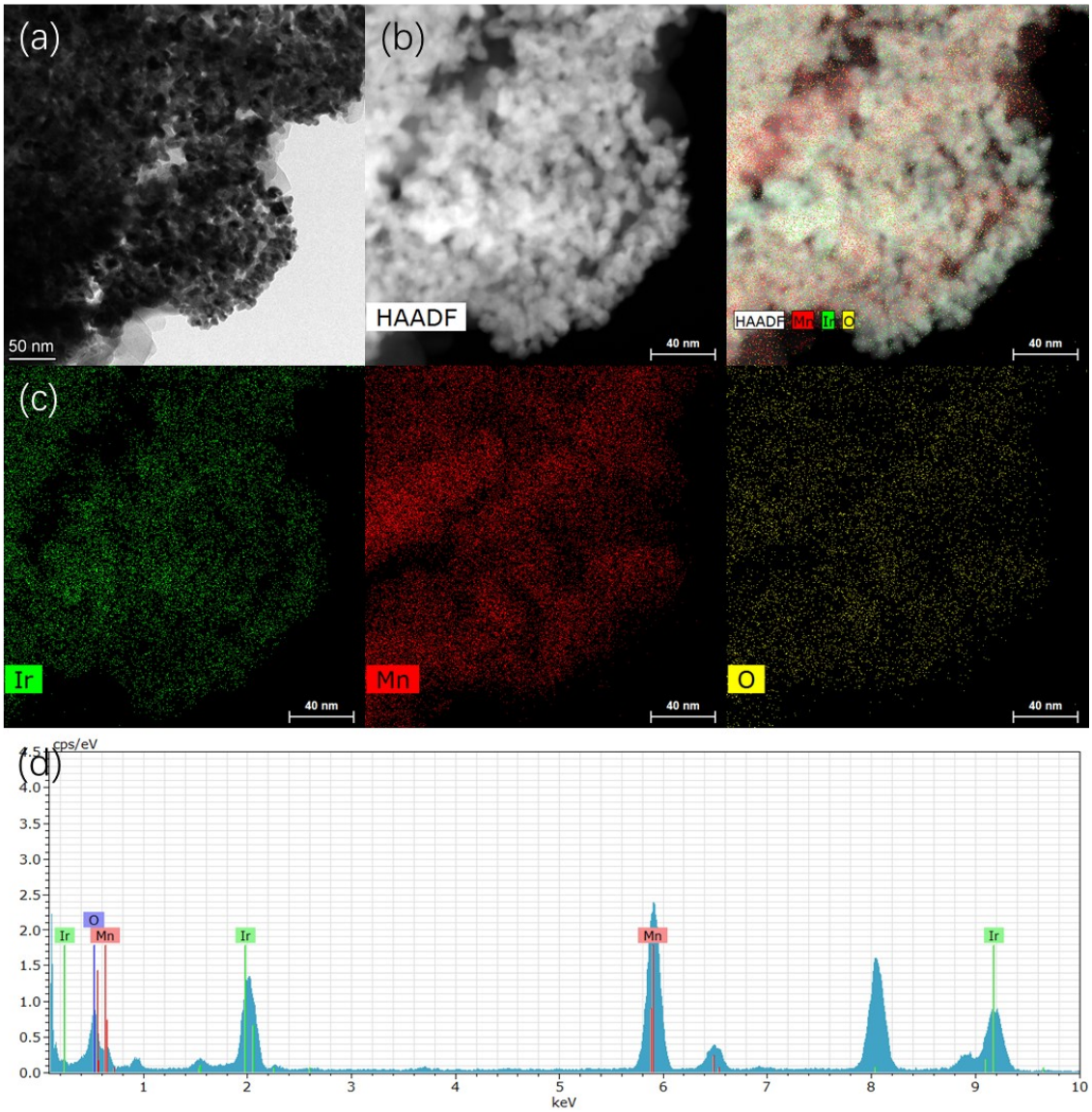

Figure S4 TEM (a), HAADF-STEM (b), HAADF-STEM mapping (c) and atomic ratio of Ir, Mn and O (d) of $Ir_{0.2}Mn_{0.8}O_y$ hybrids.

It can be seen from the high-angle annular dark-field scanning transmission electron microscopy (HAADF-STEM) in Fig. S4a (ESI†), the particle size of the nanoparticles is about 10 nm. The distribution of Ir, Mn and O elements are very uniform in electrodes surface (Fig. S4 b-c, ESI†), and the molar ratio is 7.2:63.1:29.7 (Fig. S4d, ESI†).

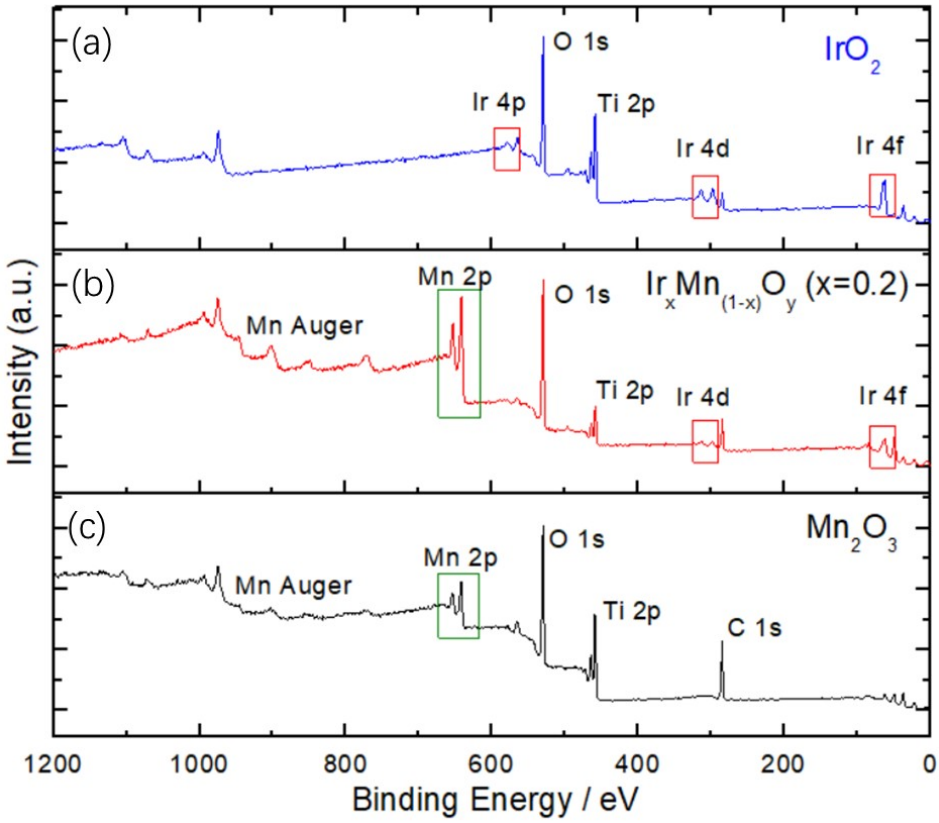

Figure S5 The XPS survey spectra of IrO_2 (a), $Ir_{0.2}Mn_{0.8}O_y$ hybrids (b) and Mn_2O_3 (c).

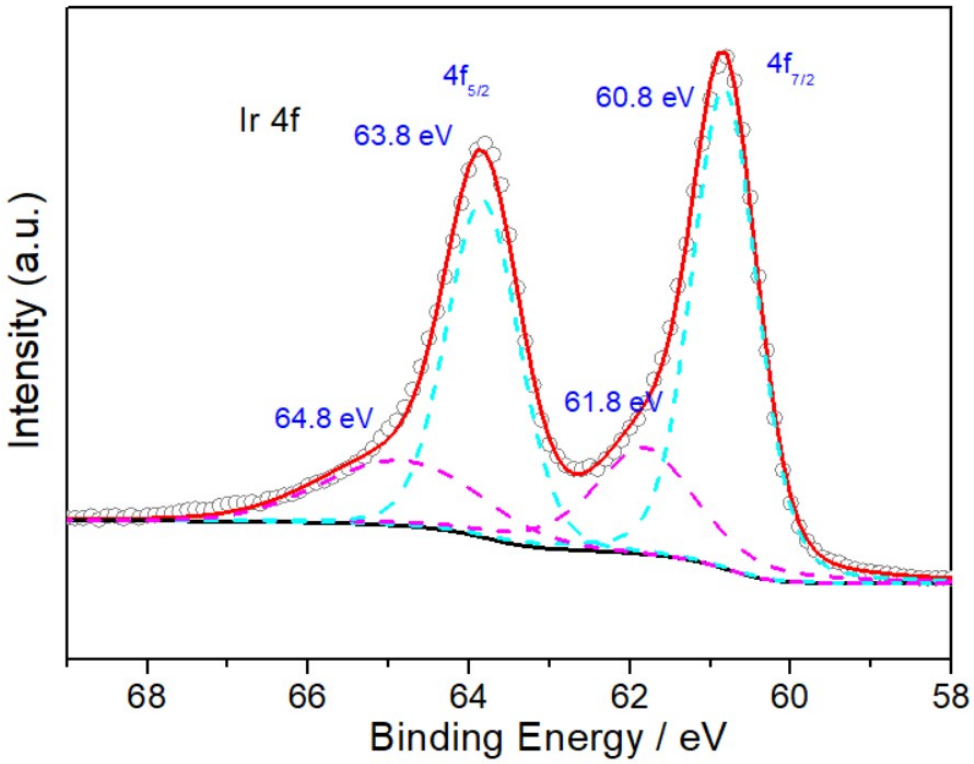

Figure S6 The XPS core-level spectra of Ir 4f of metal Ir.

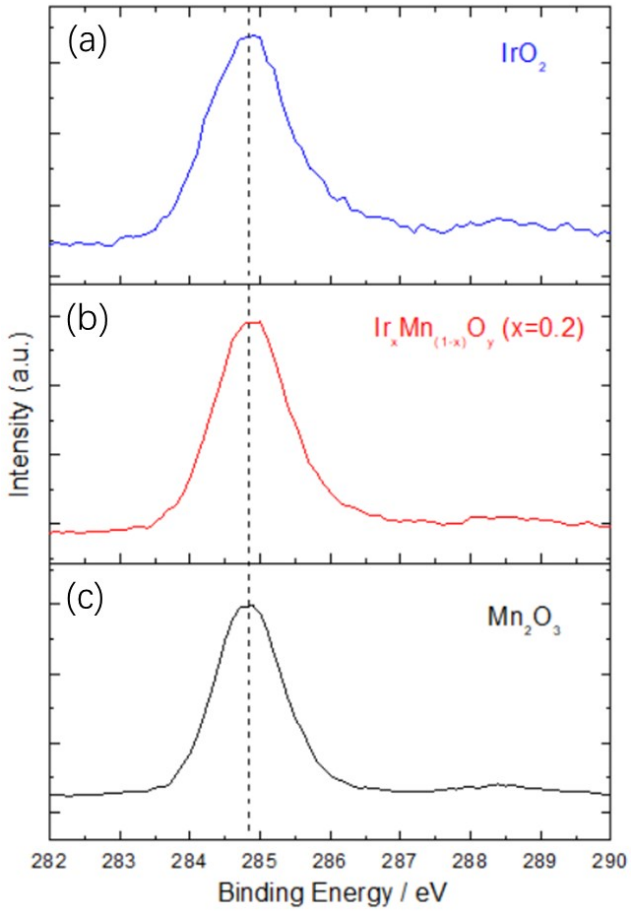

Figure S7 The XPS core-level spectra of C 1s of IrO_2 (a), $Ir_{0.2}Mn_{0.8}O_y$ hybrids (b) and Mn_2O_3 (c).

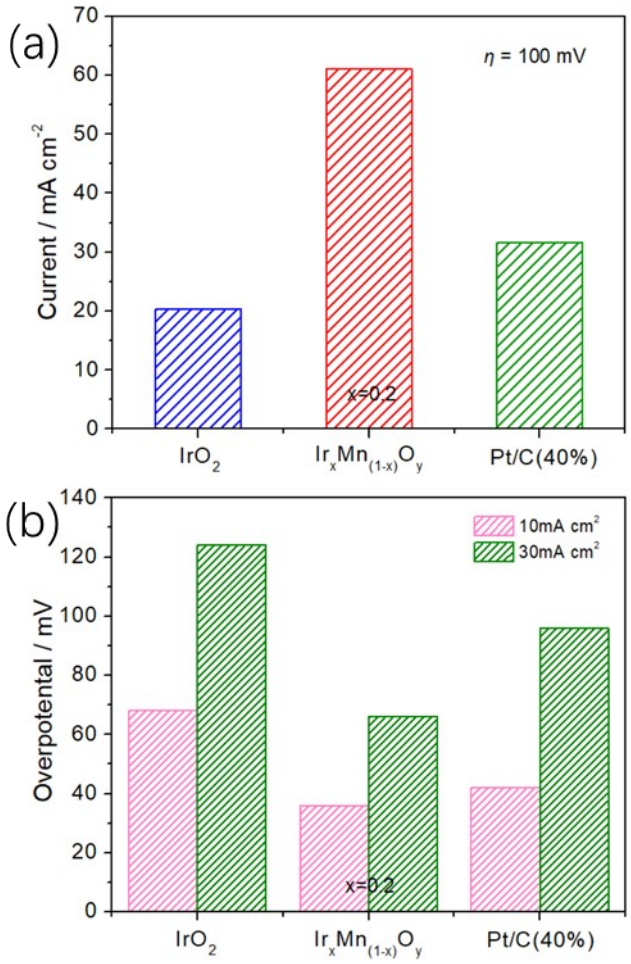

Figure S8 The apparent HER activities of IrO_2, $Ir_{0.2}Mn_{0.8}O_y$ hybrids and Pt/C at an overpotential of 100 mV in 0.5 M H_2SO_4 (a). Overpotentials of HER of IrO_2, $Ir_{0.2}Mn_{0.8}O_y$ hybrids and Pt/C at apparent current densities of 10 and 30 mA cm^{-2} (b) in 0.5 M H_2SO_4.

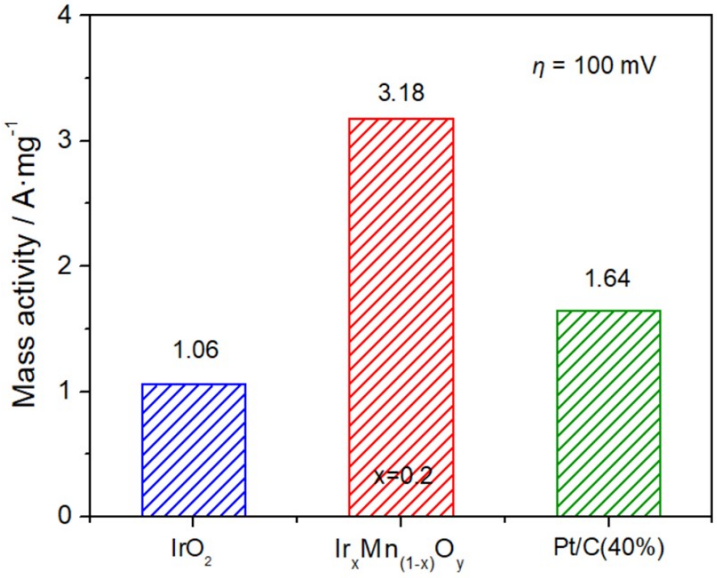

Figure S9 The mass activities of HER of IrO_2, $Ir_{0.2}Mn_{0.8}O_y$ hybrids and Pt/C at an overpotential of 100 mV in 0.5 M H_2SO_4.

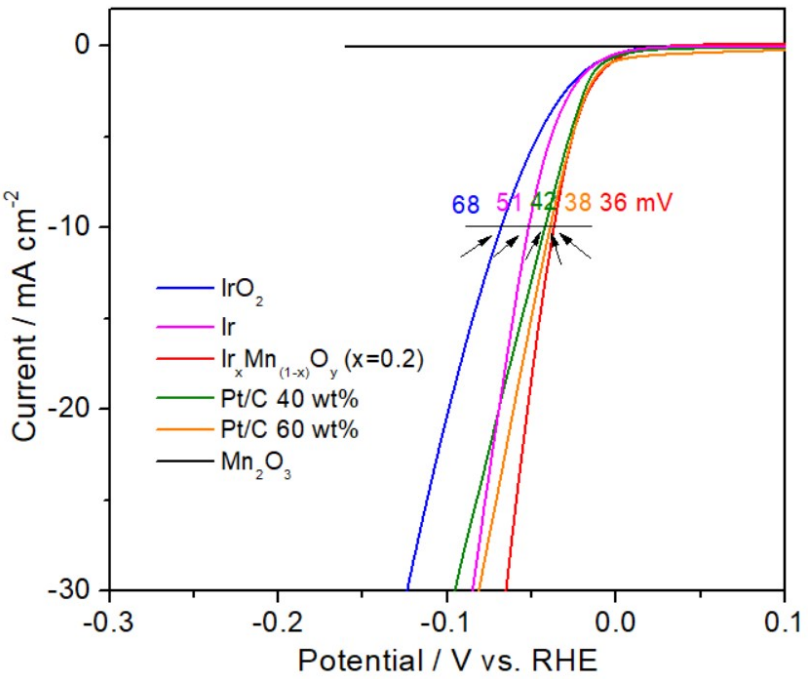

Figure S10 The apparent HER activities of IrO_2, Ir, $Ir_{0.2}Mn_{0.8}O_y$ hybrids, 40 wt% Pt/C, 60 wt% Pt/C and Mn_2O_3 in 0.5 M H_2SO_4.

The loading of platinum in 60 wt% Pt/C is 1.5 times that of 40 wt% Pt/C, so the HER activity of 60 wt% Pt/C is better than that of 40 wt% Pt/C. The overpotential of 60 wt% Pt/C is 38 mV to obtain the apparent current density of 10 mA cm^{-2}. However, the HER activity of 60 wt% Pt/C is still lower than that of $Ir_{0.2}Mn_{0.8}O_y$ hybrids, even though the noble metal loading of 60 wt% Pt/C is 1.5 times that of $Ir_{0.2}Mn_{0.8}O_y$ hybrids. The above results have indicated that $Ir_{0.2}Mn_{0.8}O_y$ hybrids does exhibit the excellent HER activity in acidic system, especially at very low loading.

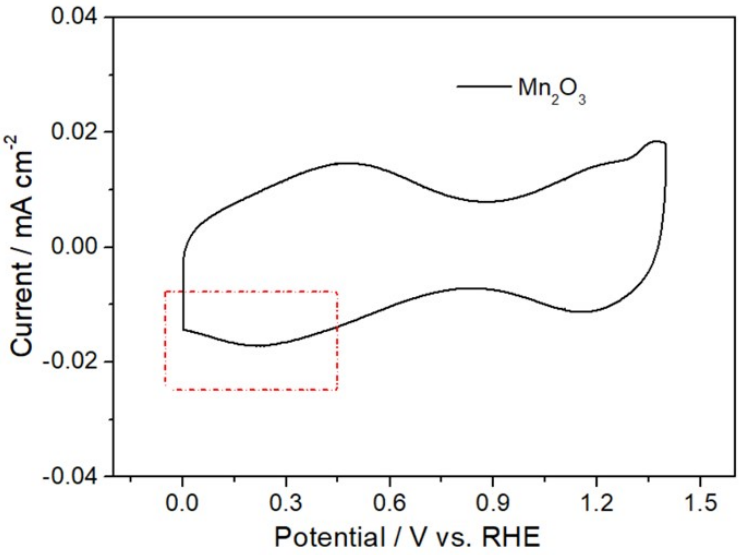

Figure S11 The cyclic voltammetry curve of Mn_2O_3 in 0.5 M H_2SO_4.

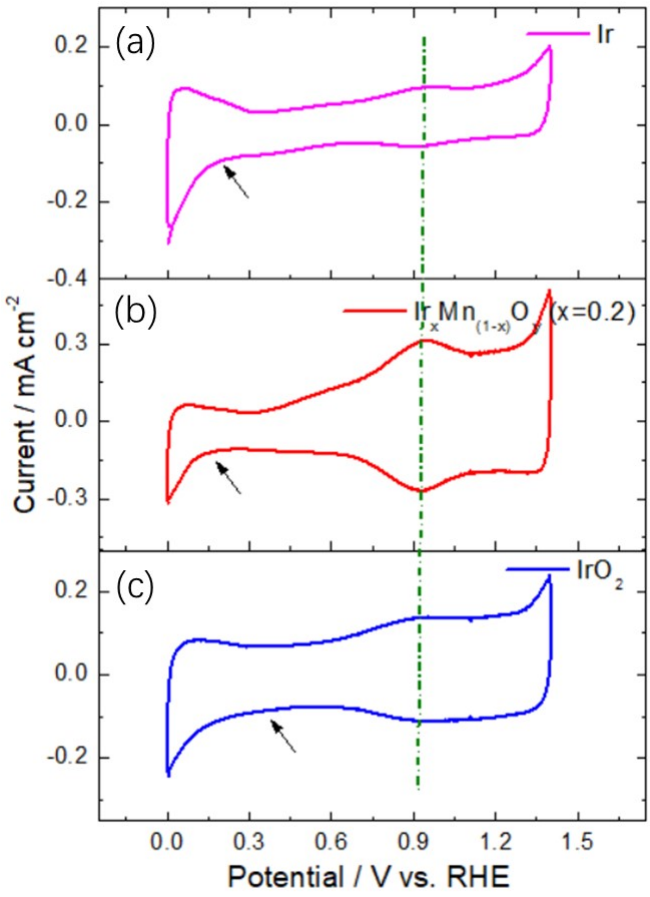

Figure S12 The cyclic voltammetry curves of Ir (a), $Ir_{0.2}Mn_{0.8}O_y$ hybrids (b) and IrO_2 (c) in 0.5 M H_2SO_4.

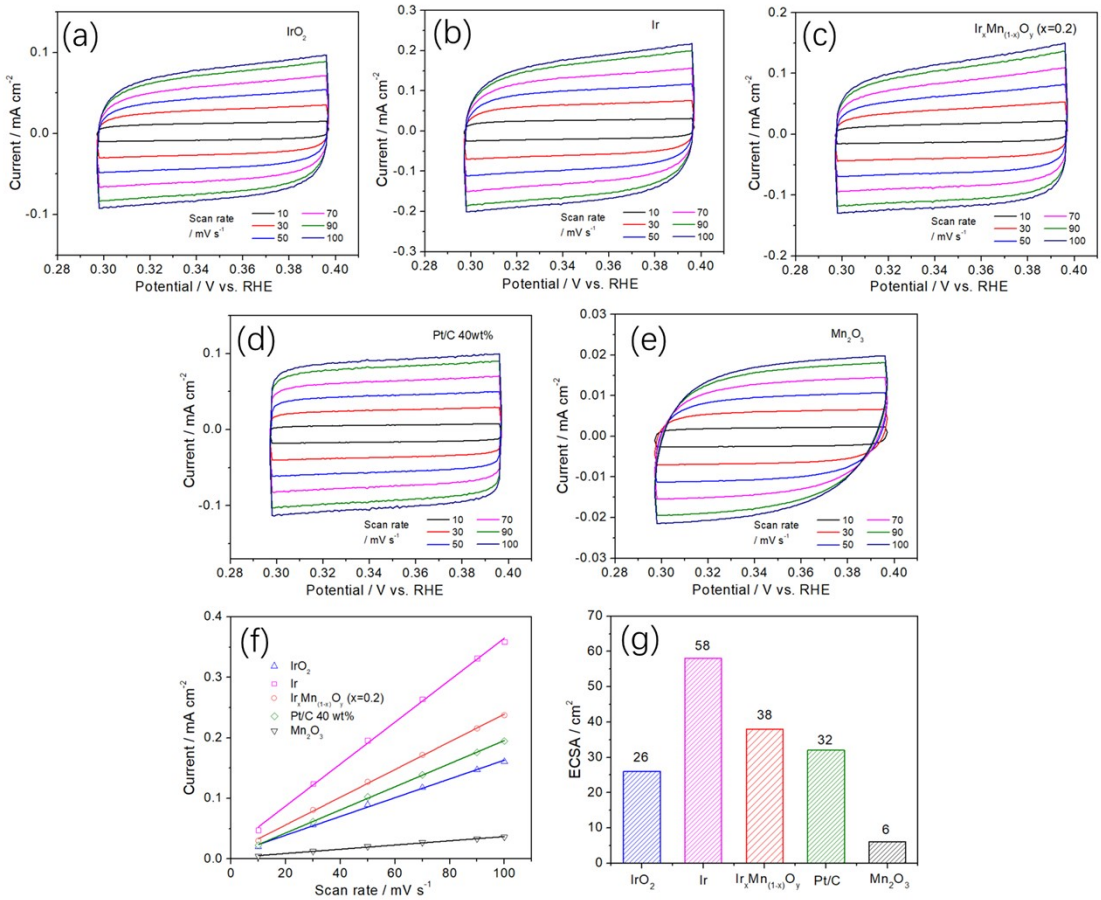

Figure S13 The double-capacitance curves of IrO_2 (a), Ir (b), $Ir_{0.2}Mn_{0.8}O_y$ hybrids (c), Pt/C (d) and Mn_2O_3 (e) under different sweeping speeds in 0.5 M H_2SO_4. The double layer capacitance fitting curves of IrO_2, Ir, $Ir_{0.2}Mn_{0.8}O_y$ hybrids, Pt/C and Mn_2O_3 (f). The electrochemical surface areas (ECSAs) of IrO_2, Ir, $Ir_{0.2}Mn_{0.8}O_y$ hybrids, Pt/C and Mn_2O_3 (g).

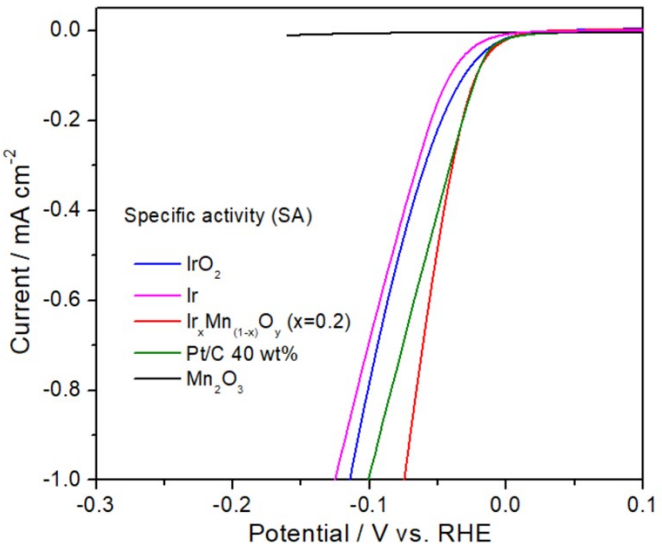

Figure S14 The specific activities (SAs) of IrO_2, Ir, $Ir_{0.2}Mn_{0.8}O_y$ hybrids, Pt/C and Mn_2O_3 in 0.5 M H_2SO_4.

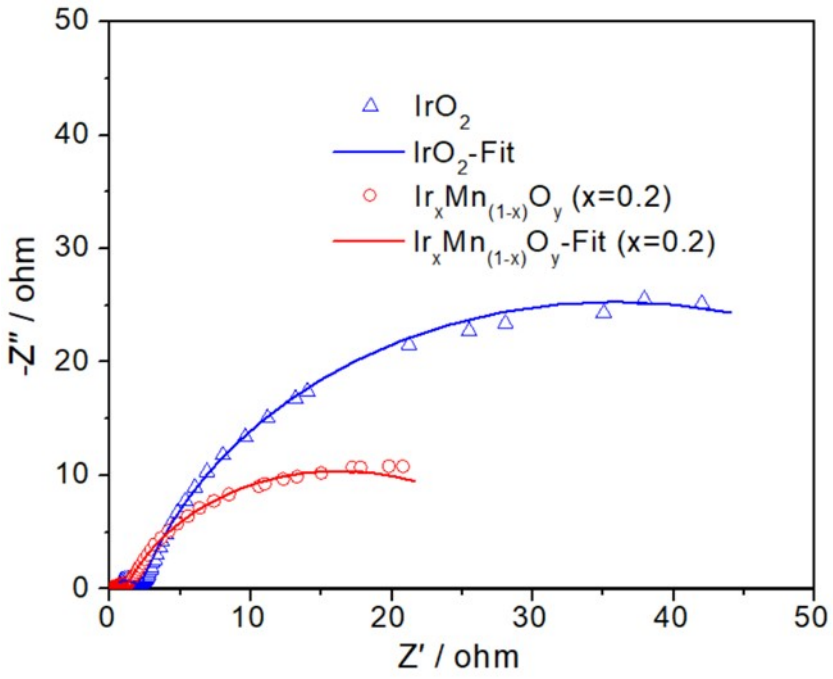

Figure S15 The EIS measurements of of $Ir_{0.2}Mn_{0.8}O_y$ hybrids and IrO_2 at η = 10 mV in 0.5 M H_2SO_4.

Fig. S15 (ESI†) are the Nyquist plots of $Ir_{0.2}Mn_{0.8}O_y$ hybrids and IrO_2 at the overpotential of 10 mV. Equivalent circuit fitted by Zview software ($R_s(R_fC_f)(R_{ct}C_{dl})$). The R_s (the solution resistance) of $Ir_{0.2}Mn_{0.8}O_y$ hybrids and IrO_2 electrodes are almost the same, which are 0.287 and 0.281 Ω cm^2, respectively. But for R_{ct} (the charge transfer resistance), the R_{ct} of $Ir_{0.2}Mn_{0.8}O_y$ hybrids is 30.36 Ω cm^2, and the R_{ct} of IrO_2 is 67.56 Ω cm^2. The R_{ct} of $Ir_{0.2}Mn_{0.8}O_y$ hybrids is smaller, which indicates that the charge transfer is faster in the HER process, which is beneficial to improve the HER activity.

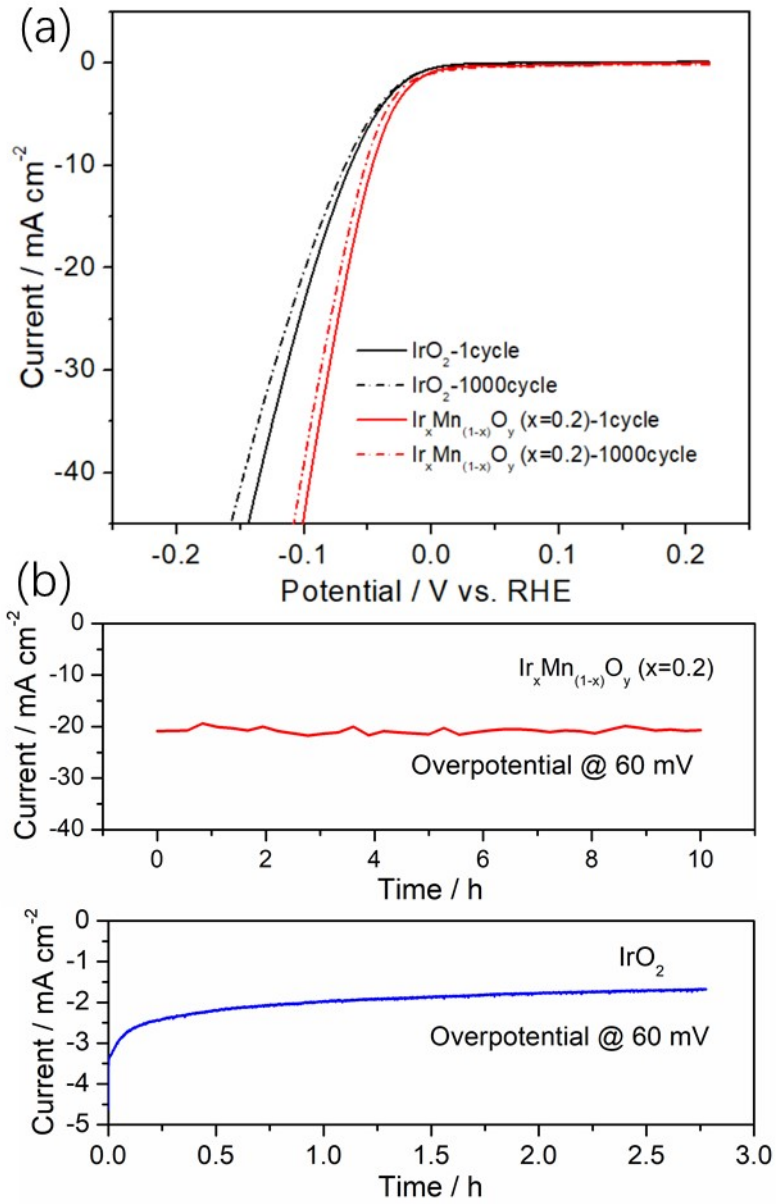

Figure S16 Accelerated life test of $Ir_{0.2}Mn_{0.8}O_y$ hybrids and IrO_2 through the consecutive CV scan measurements in 0.5 M H_2SO_4 (a). Long-time stability tests of $Ir_{0.2}Mn_{0.8}O_y$ hybrids (b) and IrO_2 (c) at the overpotential of 60 mV in 0.5 M H_2SO_4.

Fig. S16 (ESI†) is the accelerated life test of the $Ir_{0.2}Mn_{0.8}O_y$ hybrids electrode. After 1000 cycles of CV scanning, the HER activity of the $Ir_{0.2}Mn_{0.8}O_y$ hybrids decreased slightly, which was obviously better than that of IrO_2 electrode in Fig. S16a (ESI†). After 10 h of chronoamperometry testing at the overpotential of 60 mV, the activity of HER decreased by only 0.91% (from 20.91 to 20.72 mA cm^{-2}) for $Ir_{0.2}Mn_{0.8}O_y$ hybrids electrode in Fig. S16b (ESI†). For IrO_2, its stability of chronoamperometry testing is much worse in Fig. S16c (ESI†).

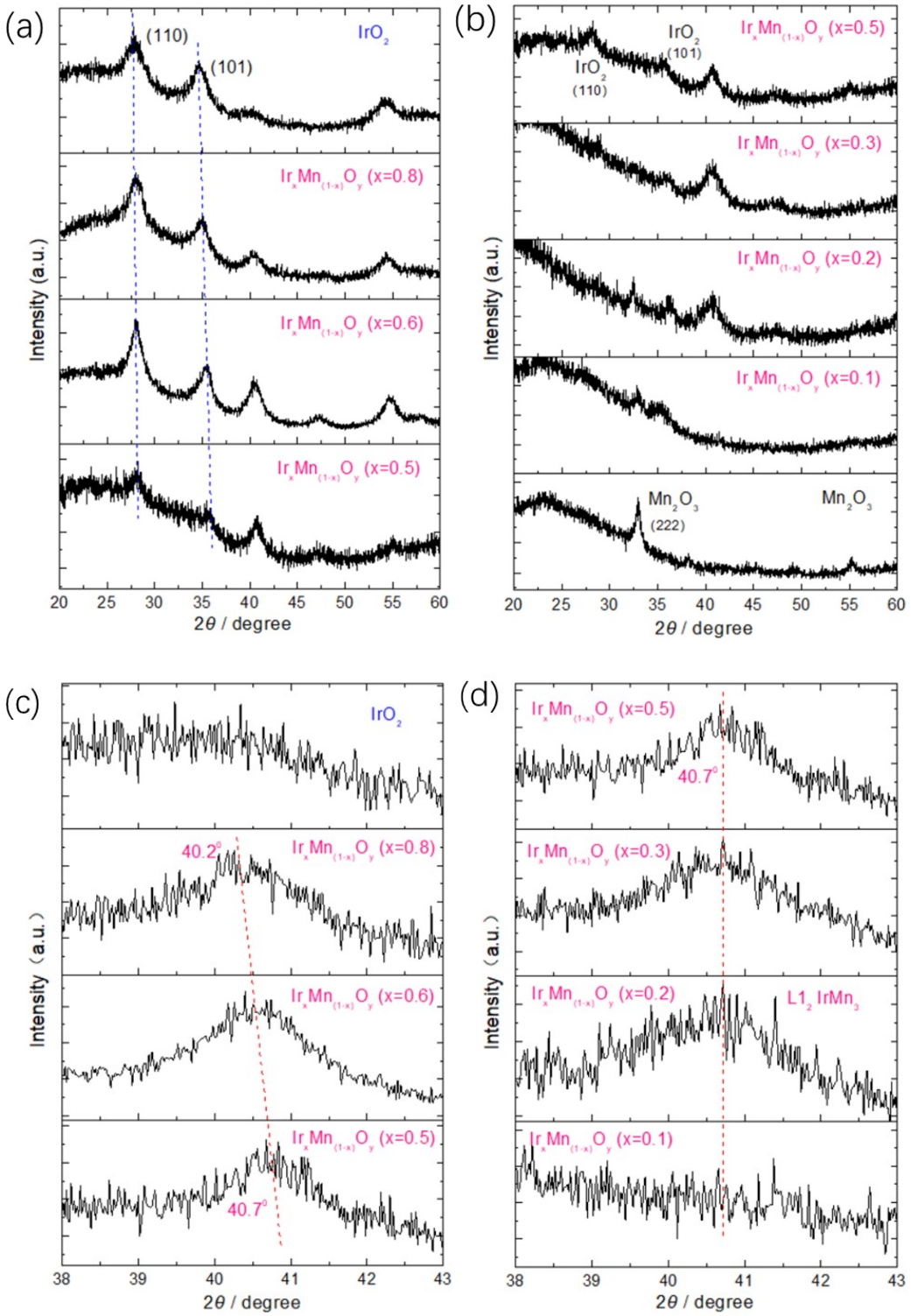

Figure S17 X-ray diffraction patterns of IrO_2 and $Ir_xMn_{(1-x)}O_y$ hybrids (x=0.8, 0.6 and 0.5) (a). X-ray diffraction patterns of $Ir_xMn_{(1-x)}O_y$ hybrids (x=0.5, 0.3, 0.2 and 0.1) and Mn_2O_3 (b). X-ray diffraction patterns of $Ir_xMn_{(1-x)}O_y$ hybrids with different x content in range of 38 ~ 43° ((c) x > 0.5; (d) x < 0.5).

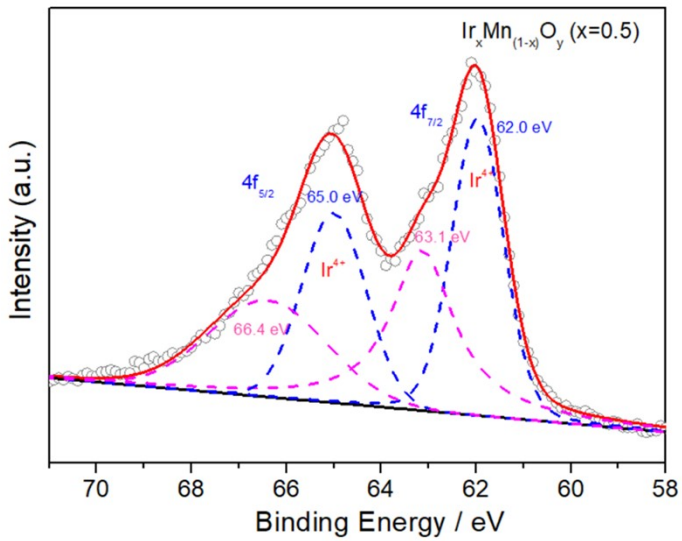

Figure S18 The XPS core-level spectra of Ir 4f of the $Ir_xMn_{(1-x)}O_y$ hybrids (x = 0.5).

At first, as shown in Fig. S17a (ESI†), there are obvious (110) and (101) crystal planes of IrO_2 in XRD patterns of $Ir_xMn_{(1-x)}O_y$ hybrids (x > 0.5). It can also be found that with the addition of Mn, the (110) and (101) crystal planes of IrO_2 continuously move forward. Especially for the (101) crystal plane, it has been positively moved from 34.6° (x = 1.0) to 35.7° (x = 0.5). This is due to the insertion of Mn atoms into the lattice of IrO_2. But the (110) and (101) crystal planes of IrO_2 are no longer obvious in $Ir_xMn_{(1-x)}O_y$ hybrids (x < 0.5) in Fig. S17b (ESI†). Therefore, IrO_2 is no longer the active center, for $Ir_xMn_{(1-x)}O_y$ hybrids (x < 0.5). Secondly, an obvious diffraction peak appears at 40.2° in Fig. S17a (ESI†), which cannot be clearly observed in the XRD pattern of IrO_2. Further, it can be found by carefully observing in Fig. S17c (ESI†) that the diffraction peak at 40.2° will continue to be shifted with the addition of Mn. It can be found that the diffraction peak shifts from 40.2° (x = 1.0) to 40.7° (x = 0.5). However, in Fig. S17d (ESI†), the diffraction peak is no longer moved, but is fixed to 40.7° (x < 0.5). When the Mn content is high, the newly formed diffraction peak should be attributed to the special characteristic diffraction peak of $Ir_xMn_{(1-x)}O_y$ hybrids. According to previous literature, the diffraction peak near 41° can correspond to Ir(111) or MnO(222) crystal plane, and can also be attributed to $IrMn_3$(111) crystal plane. If the metal Ir is regarded as the active center, there will be a contradiction. The specific contradiction is that from x=0.5 to x=0.1, the amount of H_2IrCl_6 added is gradually reduced, so the formed metal Ir is also gradually reduced. If the metal Ir is the active center, the activity of the $Ir_xMn_{(1-x)}O_y$ hybrids (x < 0.5) should decrease gradually, but this is contrary to the experimental results. At the same time, XPS results have shown that when x=0.5, there is no metallic Ir on the surface of $Ir_xMn_{(1-x)}O_y$ hybrids, but an oxidized Ir (Fig. S18, ESI†). Only when x=0.2, Ir^{0+} 4f has already appeared in XPS spectra of $Ir_xMn_{(1-x)}O_y$ hybrids in Fig. 2a. Therefore, when x<0.5, it can be considered as a process of gradually forming $IrMn_3$ phase with the increase of Mn content. With the formation of $IrMn_3$ phase, HER activity is

increasing, so it is presumed to be the real active center. For $Ir_xMn_{(1-x)}O_y$ hybrids (x = 0.1), because of the high Mn content and low Ir content, the $IrMn_3$ phase can not be effectively formed, so the HER activity drops sharply.

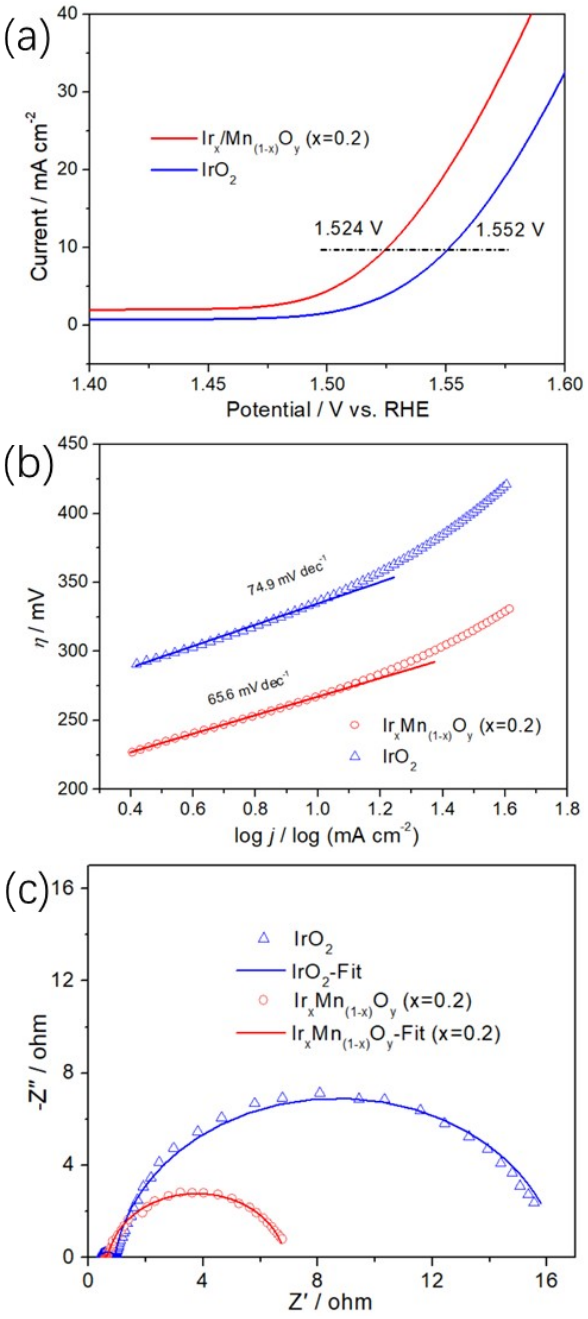

Figure S19 The OER activities (a) and Tafel slopes (b) of $Ir_{0.2}Mn_{0.8}O_y$ hybrids and IrO_2 in 0.5 M H_2SO_4. The EIS measurements of $Ir_{0.2}Mn_{0.8}O_y$ hybrids and IrO_2 at overpotential of 300 mV in 0.5 M H_2SO_4 (c).

As shown in Fig. S19 (ESI†), the OER activity of $Ir_{0.2}Mn_{0.8}O_y$ hybrids is better than that of IrO_2 electrode. At the same time, the Tafel slope (65.6 mV dec^{-1}) and electrochemical transfer resistance (6.15 Ω cm^2) of $Ir_{0.2}Mn_{0.8}O_y$ hybrids are lower than those of IrO_2 electrode (74.9 mV dec^{-1} and 15.53 Ω cm^2). The above analysis indicates that the $Ir_{0.2}Mn_{0.8}O_y$ hybrids has excellent OER activity.

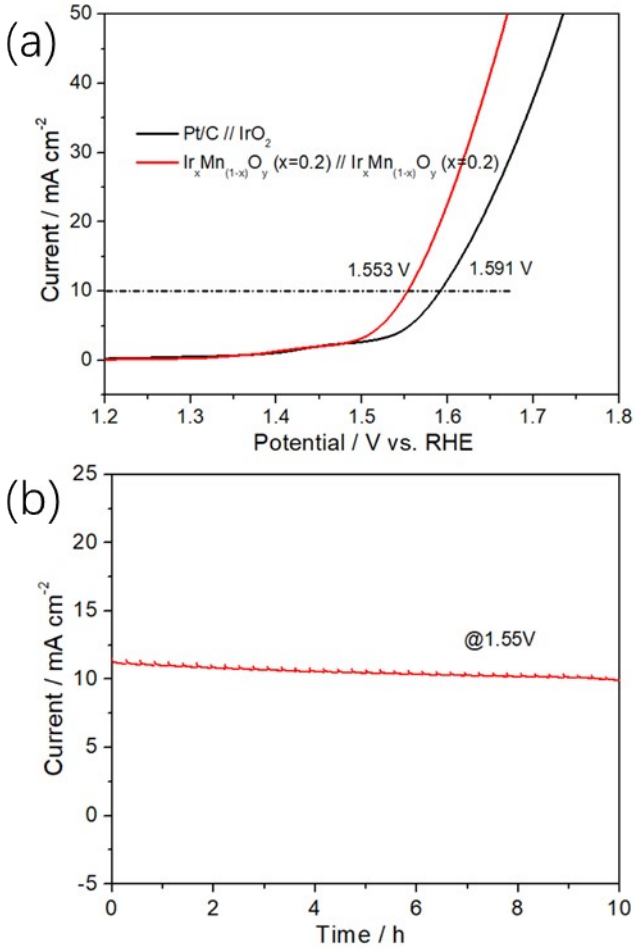

Figure S20 The overall water splitting capabilities of $Ir_xMn_{(1-x)}O_y$ (x=0.2) // $Ir_xMn_{(1-x)}O_y$ (x=0.2) and Pt/C // IrO_2 in 0.5 M H_2SO_4 solution (a). The overall water splitting stability of $Ir_xMn_{(1-x)}O_y$ (x=0.2) (Load: 0.02 mg cm^{-2}) // $Ir_xMn_{(1-x)}O_y$ (x=0.2) (Load: 0.1 mg cm^{-2}) in 0.5 M H_2SO_4 solution (b).

Further, in order to verify the overall water splitting capability, in 0.5 M H_2SO_4 solution, a two-electrode system with $Ir_{0.2}Mn_{0.8}O_y$ hybrids electrodes as anode and cathode was constructed, denoted as $Ir_xMn_{(1-x)}O_y$ hybrids // $Ir_xMn_{(1-x)}O_y$ hybrids. A comparative evaluation of Pt/C // IrO_2 water electrolyzer composed of Pt/C (cathode) and IrO_2 (anode) was carried out. The recorded polarization curves in Fig. S20a (ESI†) indicate that the $Ir_xMn_{(1-x)}O_y$ hybrids // $Ir_xMn_{(1-x)}O_y$ hybrids require a lower voltage of 1.553 V to achieve 10 mA cm^{-2}, smaller than 1.591 V required for Pt/C // IrO_2. Moreover, when the applied voltage is set at 1.56 V, a constant current density of 10 mA cm^{-2} is well maintained for 10 h in Fig. S20b (ESI†).

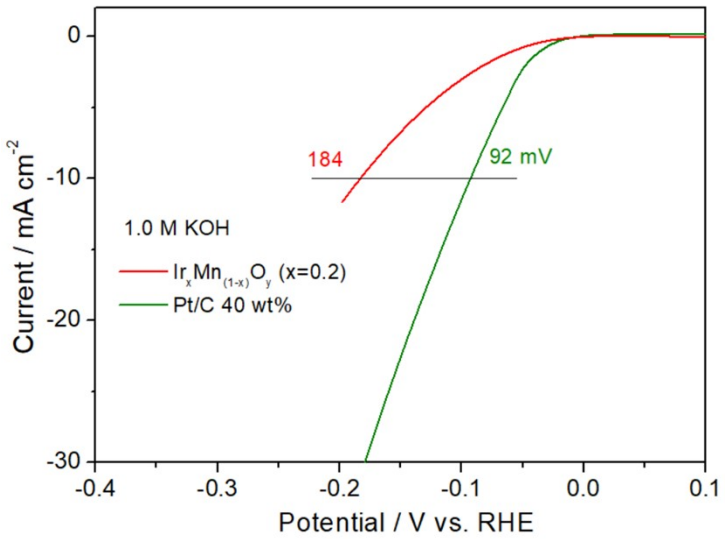

Figure S21 The apparent HER activities of $Ir_{0.2}Mn_{0.8}O_y$ hybrids and 40 wt% Pt/C in 1.0 M KOH.

The HER activity of $Ir_xMn_{(1-x)}O_y$ hybrids in alkaline solution has also been tested. However, the HER activity of $Ir_xMn_{(1-x)}O_y$ in alkaline solution is not ideal. At the apparent current density of 10 mA cm^{-2}, the overpotentials of $Ir_{0.2}Mn_{0.8}O_y$ hybrids and Pt/C electrodes is 184 and 92 mV, respectively. Here, the performance of $Ir_{0.2}Mn_{0.8}O_y$ hybrid is obviously worse than that of Pt/C. This is because it is more difficult to break the HO-H bond in H_2O to get hydrogen intermediate in alkaline solution than that in acid solution. For $Ir_{0.2}Mn_{0.8}O_y$ hybrids, the adsorption energy of H was modified through the formation of $L1_2$-$IrMn_3$ phase, the acidic HER activity was improved. However, its ability to destroy HO-H bond in alkaline solution has not been improved, so its alkaline HER activity is poor.

Table S1 Composition analysis of $Ir_xMn_{(1-x)}O_y$ hybrids with different Ir-Mn ratios by XRF

$Ir_xMn_{(1-x)}O_y$	Consumption / mol%		Content / mol%	
hybrids	Ir	Mn	Ir	Mn
x=0.2	20	80	20.020	79.980
x=0.3	30	70	37.839	62.161
x=0.5	50	50	45.851	54.149
x=0.6	60	40	74.109	25.891
x=0.8	80	20	80.380	19.620
x=0.9	90	10	93.856	6.144

According to XPS test results, for $Ir_xMn_{(1-x)}O_y$ hybrids (x=0.2), the atomic ratio of Ir and Mn is 1.76:19.08. The molar ratio of Ir-Mn near the electrode surface is obviously lower than those of STEM-mapping and XRF, which indicates that Mn is obviously enriched on the surface.

Table S2. Comparison of HER activities between optimized $Ir_xMn_{(1-x)}O_y$ hybrids (x=0.2) and other ultra-low load Ir-based electrocatalysts in literatures.

Catalyst	**Electrolyte**	**Ir Loading ($\mu g\ cm^{-2}$)**	**η_{10} (mV)**	**Tafel slope mV dec^{-1}**	**References**
$Ir_xMn_{(1-x)}O_y$ hybrids (x=0.2)	**0.5 M H_2SO_4**	**19.2**	**36**	**31.6**	**This work without iR-compensation**
Ir-NCNSs	0.5 M H_2SO_4	2.54	46.3	52	ACS Appl. Mater. Interfaces, 2021, 13, 22448−22456. **(1)** without iR-compensation
IrNiTa/Si	0.5 M H_2SO_4	8.14	99	35	Adv. Mater., 2020, 32, 1906384. **(2)**
AuIr@CNT	0.5 M H_2SO_4	14.3	27.3	30.2	J. Mater. Chem. A, 2020, 8, 20168–20174. **(3)** without iR-compensation
Au@$AuIr_2$	0.5 M H_2SO_4	20	29	15.6	J. Am. Chem. Soc., 2021, 143, 4639−4645. **(4)** 90% iR-compensation
CB[6]-Ir2	0.5 M H_2SO_4	20	54	30	ACS Energy Lett., 2019, 4, 1301−1307. **(5)** 100% iR-compensation
np-$Ir_{70}Ni_{30}$	0.5 M H_2SO_4	20.24	35.2	43	ACS Nano, 2021, 15, 5333−5340. **(6)** iR-compensation
Ir_VG	0.5 M H_2SO_4	50	47	43	J. Mater. Chem. A, 2019, 7, 20590–20596. **(7)**
Ir-NS	0.5 M H_2SO_4	71	31	17.2	Chem. Commun., 2021, 57, 8620–8623. **(8)**

References

1. X. Wu, Z. Wang, K. Chen, Z. Li, B. Hu, L. Wang and M. Wu, Unravelling the Role of Strong Metal−Support Interactions in Boosting the Activity toward Hydrogen Evolution Reaction on Ir Nanoparticle/N-Doped Carbon Nanosheet Catalysts, *ACS Appl. Mater. Interfaces*, 2021, 13, 22448−22456.

2. Z.-J. Wang, M.-X. Li, J.-H. Yu, X.-B. Ge, Y.-H. Liu, W.-H. Wang, Low-Iridium-Content IrNiTa Metallic Glass Films as Intrinsically Active Catalysts for Hydrogen Evolution Reaction. *Adv. Mater.*, 2020, 32, 1906384.

3. H. Hu, F. M. D. Kazim, Z. Ye, Y. Xie, Q. Zhang, K. Qu, J. Xu, W. Cai, S. Xiao and Z. Yang, Electronically delocalized Ir enables efficient and stable acidic water splitting, *J. Mater. Chem. A*, 2020, 8, 20168–20174.

4. H. Wang, Z. Chen, D. Wu, M. Cao, F. Sun, H. Zhang, H. You, W. Zhuang and R. Cao, Significantly Enhanced Overall Water Splitting Performance by Partial Oxidation of Ir through Au Modification in Core–Shell Alloy Structure, *J. Am. Chem. Soc.*, 2021, 143, 4639−4645.

5. H. You, D. Wu, Z. Chen, F. Sun, H. Zhang, Z. Chen, M. Cao, W. Zhuang and R. Cao, Highly Active and Stable Water Splitting in Acidic Media Using a Bifunctional Iridium/Cucurbit[6]uril Catalyst, *ACS Energy Lett.*, 2019, 4, 1301−1307.

6. Y. Yu, K. Jiang, M. Luo, Y. Zhao, J. Lan, M. Peng, F. M. F. de Groot and Y. Tan, Self-Activated Catalytic Sites

on Nanoporous Dilute Alloy for High-Efficiency Electrochemical Hydrogen Evolution, *ACS Nano*, 2021, 15, 5333−5340.

7. S. B. Roy, K. Akbar, J. H. Jeon, S.-K. Jerng, L. Truong, K. Kim, Y. Yi and S.-H. Chun, Iridium on vertical graphene as an all-round catalyst for robust water splitting reactions, *J. Mater. Chem. A*, 2019, 7, 20590–20596.

8. Y. Xie, X. Long, X. Li, C. Chang, K. Qu and Z. Yang, The template synthesis of ultrathin metallic Ir nanosheets as a robust electrocatalyst for acidic water splitting, *Chem. Commun.*, 2021, 57, 8620–8623.